PNAS

Proceedings of the National Academy of Sciences of the United States of America

This is the peer-reviewed version of the following article:

which will be published in final form at:

http://www.pnas.org/

A comprehensive structural model of the mechanochemical cycle of a mitotic motor highlights molecular adaptations in the kinesin family

Adeline Goulet[1,4], Jennifer Major[2], Yonggun Jun[3], Steven P. Gross[3], Steven S. Rosenfeld[2], Carolyn A. Moores[1*]

[1] *Institute of Structural and Molecular Biology, Birkbeck College, London, WC1E 7HX, UK*

[2] *Department of Cancer Biology, Lerner Research Institute, Cleveland Clinic, Cleveland, OH 44195, USA*

[3] *Department of Developmental and Cell Biology, University of California, Irvine, California 92697, USA*

[4] *Current address: Architecture et Fonction des Macromolécules Biologiques, Unité Mixte de Recherche 7257 Centre National de la Recherche Scientifique and Aix-Marseille University, 13288 Marseille Cedex 09, France*

** Corresponding author:*

E-mail: c.moores@mail.cryst.bbk.ac.uk
Tel: +44 207 631 6858
Fax: +44 207 631 6803

A comprehensive structural model of the mechanochemical cycle of a mitotic motor highlights molecular adaptations in the kinesin family

Adeline Goulet[1,4], Jennifer Major[2], Yonggun Jun[3], Steven P. Gross[3], Steven S. Rosenfeld[2], Carolyn A. Moores[1*]

[1] *Institute of Structural and Molecular Biology, Birkbeck College, London, WC1E 7HX, UK*

[2] *Department of Cancer Biology, Lerner Research Institute, Cleveland Clinic, Cleveland, OH 44195, USA*

[3] *Department of Developmental and Cell Biology, University of California, Irvine, California 92697, USA*

[4] *Current address: Architecture et Fonction des Macromolécules Biologiques, Unité Mixte de Recherche 7257 Centre National de la Recherche Scientifique and Aix-Marseille University, 13288 Marseille Cedex 09, France*

** Corresponding author:*
Carolyn A. Moores
Institute of Structural and Molecular Biology,
Department of Biological Sciences,
Birkbeck College,
Malet Street,
London WC1E 7HX
UK
Tel: +44 207 631 6858
E-mail: c.moores@mail.cryst.bbk.ac.uk

Classification: BIOLOGICAL SCIENCES; Biophysics and Computational Biology

Keywords: cryo-electron microscopy/ kinesins/ mechanochemistry/ microtubules/ mitosis

41,047 CHARACTERS INCLUDING SPACES

ABSTRACT

Kinesins are responsible for a wide variety of microtubule-based, ATP-dependent functions. Their motor domain drives these activities but the molecular adaptations that specify these diverse and essential cellular activities are poorly understood. It has been assumed that the first identified kinesin - the transport motor kinesin-1 – is the mechanistic paradigm for the entire superfamily, but accumulating evidence suggests that this is not the case. To address the deficits in our understanding of the molecular basis of functional divergence within the kinesin superfamily, we studied kinesin-5s, which are essential mitotic motors whose inhibition blocks cell division. Using cryo-electron microscopy and subnanometer resolution structure determination, we have visualised conformations of microtubule-bound human kinesin-5 motor domain at successive steps in its ATPase cycle. Following ATP hydrolysis, nucleotide-dependent conformational changes in the active site are allosterically propagated into rotations of the motor domain and uncurling of the drug-binding loop L5. In addition, the mechanical neck-linker element that is crucial for motor stepping undergoes discrete, ordered displacements. We also observed large reorientations of the motor N-terminus that indicate its importance for kinesin-5 function through control of neck-linker conformation. A kinesin-5 mutant lacking this N-terminus is enzymatically active, and ATP-dependent neck-linker movement and motility is defective although not ablated. All these aspects of kinesin-5 mechanochemistry are distinct from kinesin-1. Our findings directly demonstrate the regulatory role of the kinesin-5 N-terminus in collaboration with the motor's structured neck-linker, and highlight the multiple adaptations within kinesin motor domains that tune their mechanochemistries according to distinct functional requirements.

SIGNIFICANCE

Kinesins are a superfamily of ATP-dependent motors that are important for a wide variety of microtubule-based functions in eukaryotic cells. Kinesins have evolved to allow variable tuning of their motor properties, but the link between molecular variation and motor function is largely unknown. To understand this link, we have studied an essential mitotic kinesin (kinesin-5), which is the target of anticancer drugs. We used cryo-electron microscopy to directly visualise sequential conformational changes of structural elements during the motor ATPase cycle. We have revealed the contribution of kinesin-5 specific variations to motor function, and could conclude that kinesins are indeed precisely tuned according to cellular function. This insight will be important in designing kinesin-specific inhibitors in different disease contexts.

\body

INTRODUCTION

Nucleotide triphosphates are the fuel that powers the cell's machinery. Conversion of this fuel into mechanical work – *i.e.* mechanochemistry – depends on individual machines and the functional context in which they have evolved. Indeed, elucidation of the mechanochemistry of a particular machine provides critical insight into both its functions and modes of regulation. Kinesins are a superfamily of motors that use ATP to undertake microtubule- (MT) based work. Kinesins operate throughout the cell cycle in many contexts and can generate force towards the MT plus- or minus-end, and also depolymerise MTs (1). The kinesin mechanochemical engine – the motor domain (MD) – is highly conserved, and conformational changes in the active site during the motor's ATPase cycle are transmitted to other parts of the MD to generate force (2). Most of our current knowledge about kinesin mechanochemistry comes from studies of the superfamily founding member, the transport motor kinesin-1 (K1) (2). However, accumulating evidence suggests that small modifications within kinesin MDs have profound effects on their cellular function. The molecular basis of such adaptations is largely unknown.

Our interests focus on kinesin-5s (K5s), which cross-link MTs and are essential for the formation and maintenance of bipolar mitotic spindles in most eukaryotes (3). Like K1s, K5s have an N-terminal MD followed by a neck-linker (NL) that connects the MD to the rest of the motor. However, K1s are dimeric, whereas K5 tetramerisation is mediated by the coiled-coil that follows the K5 NL and gives rise to a dumbbell-shaped molecule with pairs of MDs at either end (3, 4). But it is not simply the K5 tetrameric structure – with each MD pair taking ATP-driven steps towards the MT plus-ends (5) - that is required for its mitotic functions: K5 MDs have specific mechanochemical properties that are matched to their spindle functions (6). Typically, K5s are slow motors thought to work in teams when cross-linking and sliding MTs (5). The MT-stimulated ATPase turnover of monomeric K5 is slower than K1 (5-9/s vs ~50/s) (7-9) with phosphate release being the rate-limiting step (6-8/s) (10). K5 dimer stepping is concomitantly slower than K1 (~100 nm/s vs ~650 nm/s unloaded velocity) and has a different response to external load (11, 12).

A complete molecular explanation for these divergent properties remains elusive. Although it is well established that ATP binding induces NL docking along the MD towards the MT plus-end in plus-end kinesins, different physical properties of the NL and variations in nucleotide-dependent conformational changes affect modes

of force generation (3). Recently, the collaborative role of the K1 MD N-terminus – in particular its proximal portion, called the cover strand – has emerged. The cover strand forms a short β-sheet (the cover-neck bundle (CNB)) with the proximal section of the NL to assist docking and thus force production (13, 14). The K5 N-terminus is longer than in K1s (19 vs 9 residues) but we recently described K5 CNB formation on ATP (AMPPNP) binding (15), while a role for K5 CNB in force generation was indirectly inferred using a K1/K5 chimera (16).

Fundamental questions remain concerning the fate of the CNB throughout the kinesin ATPase cycle, and more generally about how information is conveyed from the MD catalytic center to the site of force generation at the CNB. Deciphering the K5-specific molecular mechanism is also of great interest because vertebrate K5-specific inhibitors bind to the highly variable loop L5 that regulates the K5 ATPase cycle and NL movement (17-19). These inhibitors allosterically block ATPase activity, directional movement (20, 21) arrest mitosis (22), and are currently in cancer clinical trials (3). Using cryo-electron microscopy (cryo-EM), we have addressed deficiencies in our understanding of kinesin mechanochemistry by directly visualising MT-bound K5 in its ATP hydrolysis transition and ADP bound states. Combined with our previous characterisation of the ATP binding step of MT-bound K5 (15), we provide a comprehensive picture of the molecular mechanism of K5 throughout its ATPase cycle and highlight critical molecular adaptations in comparison with other kinesins, particularly K1s. Unexpectedly, we demonstrate a role for the N-terminus beyond force generation in controlling the NL conformation of K5s throughout their ATPase cycle. We also identify the role of the short helix α0 proximal to the active site in conveying conformational changes to the N-terminus. Using biophysical methods we directly demonstrate the kinetic role of the N-terminus in assisting NL movement and hence in supporting efficient K5 activity. We also highlight intrinsic differences in the NL of K5 compared to K1 that contribute to the very different mechanochemistries of these functionally divergent motors.

RESULTS AND DISCUSSION

To obtain a comprehensive description of the conformational changes of the MT-bound human K5 MD during its ATPase cycle, we used cryo-EM and image processing to calculate 3D reconstructions of the ATP hydrolysis transition state (with ADP aluminium fluoride, ADP.AlFx) and the ADP-bound state at 9.2Å and 10Å resolution respectively (Table S1; Fig. S1). We took a number of approaches in interpreting these structures: 1) identification and tracking of critical elements in the K5 MD by localisation in 3D reconstructions and difference maps of a covalently bound undecagold label at each of three engineered cysteines at the N-terminus (A9C), L5 (T126C) and NL (V365C) (Table S1; Figs. 1A and 2A; Fig. S2) and, 2) generation of pseudo-atomic models for each nucleotide state validated by quantitative docking and consistency with the positions of the gold densities (Table S2; Figs. 1B and 2B). In each case, the asymmetric unit of these reconstructions – a K5 MD-$\alpha\beta$-tubulin dimer - is the basis of our description. This global analysis of conformational changes combines our current studies with previous work characterising the ATP-binding step (15).

The ATP hydrolysis transition state. The triangular K5 MD bound to ADP.AlFx – mimicking the ATPase hydrolysis transition state - points towards the MT plus-end (Fig. 1). The main MT binding contacts are formed by helix α4 and loop L8 (Figs. 1C-E) consistent with a tight-binding state, as previously shown for K1 (23, 24). The curved density protruding above the active site is L5 (Figs. 1A,B,D, gold density on T126C in pink), while the active site itself is occupied and compact (Fig. 1D). The N-terminus extends perpendicularly to the MD long axis, confirmed by the A9C-labelled gold density (Figs. 1A-B), and has weaker EM density relative to the rest of the MD that likely reflects its flexibility and disorder in this nucleotide state. Its unstructured conformation has never been captured in crystal structures, so we generated a model (Asn6-Gly16) that gives the best fit to the EM density and satisfies the gold density constraint (SI Text).

Although the NL is directed towards the MT plus-end, it adopts two discrete conformations. The first - in which the NL is docked along the MD - is essentially the same as that seen in AMPPNP (15, 25); the second is slightly disconnected from the MD (Fig. 1B). In support of these discrete NL conformations, the elongated density corresponding to the gold label on V365C stretches between the MD and the disconnected density (Figs. 1A-B). The relative occupancy of the disconnected NL conformation was estimated at 0.6 (SI Text). Using biophysical methods, we

previously concluded that while ATP binding produced NL docking, ATP hydrolysis leads to further redistribution of NL orientations (15), and our ADP.AlFx reconstruction is consistent with these data. Modelling of the NL conformation generated several conformational clusters, the top ranked of which corresponded to the NL docked conformation, while the second corresponds to the disconnected conformation (Fig. 1B; Fig. S3; SI Text). Based on these NL models, we estimated that the NL can shift ~13 Å at this early stage of ATP hydrolysis (Fig. 1B).

L5 uncurling and initiation of NL release as ATP hydrolysis begins. To determine conformational changes that occur as ATP hydrolysis proceeds, we compared the ADP.AlFx K5 conformation with our previous AMPPNP-bound structure (Figs. 1C-E). At the resolution of our reconstructions, any differences between these structures in the nucleotide-binding loops are subtle (Figs. 1C-E; Movie S1). Even so, these small changes are transmitted from the active site and amplified in the rest of the MD. First, a slight tilt of the MD (~6°) towards the MT lattice is seen in the ADP.AlFx structure (Figs. 1E; Fig. S4), in agreement with previous FRET experiments (8). This tilt of the MD occurs around the static helix α4 contact with the MT, and small changes are also observed in secondary structures adjacent to the active site, including helices α3 and α0 (Figs. 1C-E). In the AMPPNP reconstruction, density connects helix α0 and the switch I loop, a connection that is broken in the ADP.AlFx reconstruction (Fig. 1D). In the MD primary structure, helix α0 is preceded by the N-terminus via strand β1 (26) and offers a direct route for structural communication from the nucleotide-binding site to the motor N-terminus. Allosteric structural communication from the active site also causes larger conformational changes in the elements that regulate the motor – L5 – and control force generation - the NL and the N-terminus, which together form the CNB (15). As ATP hydrolysis is initiated, L5 moves away from the MD surface and uncurls from its arch-like structure (Figs. 1C-E; Movie S1). At the CNB, the K5 N-terminus moves ~20Å from its plus-end pointing location upon ATP hydrolysis, consistent with previous FRET data (Fig. 1B; Fig. S5) (15); this movement coincides with loosening between the NL and the body of the MD, thereby disrupting the CNB. Nevertheless, the remaining N-terminus-NL interaction is sufficient to limit major NL reorientation (Fig. 1B).

The ADP state: a view of the weakly MT-bound motor conformation. In the K5 ADP state (Fig. 2), the major MT contact points are still helix α4 and loop L8 (Figs.

2C-D). Although helix α4 is not completely modelled in the available ADP-bound K5 MD crystal structures due to the absence of MTs (26), the length of helix α4 remains constant throughout the K5 MT-bound ATPase cycle - including the ADP state - as previously shown for K1 (24). We thus modelled a full-length helix α4 (residues 279-304) in our docked K5 MD coordinates (Fig. 2C). In the active site, however, there is no obvious density corresponding to the preceding switch II loop, suggesting that it is flexible and not involved in coordinating the bound ADP (Fig. 2C). Additionally, helix α3 is elongated, causing retraction of the switch I loop (Fig. 2C). This 5-turn conformation of helix α3 is also seen in ADP-bound K5 MD crystal structures but not in any other MT-bound K5 state. Together, these two features of the ADP reconstruction - disorder of switch II and shortening of switch I - contribute to an open conformation of the active site. Above the active site, the flattened density corresponding to L5 (gold density on T126C in pink) protrudes from the MD, its tip unconnected to helix α3 (Figs. 2B-C).

The K5 N-terminus is perpendicular to the MD long axis in the ADP reconstruction (Figs. 2A-B). This conformation appears to be stable, as judged by its strong, long density that is still visible at higher density thresholds (Figs. 2B and 2D). Intriguingly, the conformation of the 19 amino acid K5 N-terminus has not been seen in any crystal structures, many of which contain ADP (26), likely due to its flexibility in solution. The stabilisation of K5-ADP N-terminus on MT association is probably due to stabilisation of helix α4, appropriate conformations of L5 and helix α0, and also electrostatic attraction between the negatively charged MT surface and the basic N-terminus (theoretical pI = 9.52). In contrast the NL, which is directed towards the MT minus end, and the C-terminus of helix α6 to which it is connected are not well defined (Fig. 2B), suggesting some flexibility. However, the fact that NL-attached gold density is readily visualised suggests that NL flexibility is only partial.

Flexibility of switch II, shortening of switch I and flexibility at the C-terminus of helix α6 (Figs. 2B-C) could loosen the helix α4-MT interaction and thus provide a structural explanation for low MT affinity, in all kinesins, in the ADP state (7, 23). However, it is not immediately obvious whether our ADP reconstruction captures the motor just before MT detachment (and immediately after Pi release, the rate-limiting step of the K5 monomer ATPase cycle (7)) or just after it reassociates with the MT. Although the loosening of the MD-MT contacts described above could be a feature of the post-hydrolysis MD conformation that leads to MT release, the large

conformational differences between the K5 MD in the ADP and ADP.AlFx reconstructions help to explain the relationship of these two structures. First, the MD in the ADP state is rotated clockwise by ~20° (Fig. 2D; Fig. S4); second, this rotation accompanies a major reorientation of the NL from a plus-end- to a minus-end-directed position. However, release of the NL away from its plus-end directed post-power stroke conformation must occur in solution: were such a conformational change to occur prior to MT release, the plus-end-directed force generation associated with ATP-induced NL docking would be reversed in a futile conformational cycle. This supports the conclusion that our ADP model represents the transient complex formed by the K5-ADP MD as it binds MTs from solution, prior to ADP release (below) (8). This idea is consistent with the conformation of the ADP-bound K5 MD crystal structure (26) - the conformation of the MD before MT re-attachment - in which the NL also points towards the MT minus-end.

Conformational changes on ADP release: ADP to rigor transition. Comparison between our previous rigor reconstruction and our ADP structure allows us to describe conformational changes that accompany the relatively rapid MT-stimulated ADP release step (~40-75/s) (7, 8). Although the K5 MD shape in the ADP and rigor states is similar (Figs. 2B and 3A), the MD is tilted towards the MT lattice by ~10° after ADP release (Figs. 3A; Fig. S4; Movie S2). Several other conformational changes occur when ADP is released to re-establish tight MT binding. At the active site, helix α3 uncoils to lengthen switch I, which in turn helps to stabilise the structured conformation of switch II (Fig. 3B). L5 collapses into the empty active site and, as previously described (15), interacts with this more extended conformation of switch I (Fig. 3B) and also contacts density associated with helix α0 (Fig. 3B). The interaction with helix α0 also provides evidence of transmission of structural information about the absence of bound nucleotide to the N-terminus and NL. The overall position of the K5 N-terminus is not substantially affected when ADP is released (Fig. 3A). However, although both the N-terminus and NL have the same orientation before and after ADP release, the apparent flexibility of each is reversed: in the ADP state, the N-terminus is more stable than the NL (Fig. 2B), while in rigor, the NL is more stable than the N-terminus, as shown by their corresponding strong and weak EM densities (Fig. 3A). The stabilisation of the NL in rigor is related to the reestablishment of complete density corresponding to helix α6. The K5 ADP-rigor transition shows no evidence of the large-scale twisting of the central β-sheet that is observed in the evolutionarily related region of myosin (27). This does not exclude

smaller changes in the kinesin β -sheet (e.g. (28)) but which are beyond the resolution of our current reconstructions.

The K5 N-terminus is required for efficient NL docking and motility. To test the idea that the K5 N-terminus plays a coordinating role in the motor's mechanochemistry, we monitored both the kinetics of ATP-induced NL docking and NL reorientation on ATP hydrolysis using K5 MD constructs labelled with tetramethyl rhodamine maleimide (TMR) and changes in TMR fluorescence (15). The first construct - described previously (15) - is a monomeric K5 MD construct that contains two reactive cysteines, at positions 256 in the MD beta core and 365 in the NL (V256C, V365C, *NT Intact)*. The second construct is similar except that the first 17 N-terminal residues have been deleted (*NT Deleted*). Their MT-activated steady state ATPase activity shows that the *NT Deleted* construct is characterized by a k_{cat} that is 53% lower (4.9 ± 0.5/s *versus* 3.2 ± 0.4/s) and a $K_{0.5,MT}$ over 5-fold larger (0.81 ± 0.26 μM *versus* 4.1 ± 1.1 μM) than *NT Intact* (Fig. S6). Mixing TMR-labelled *NT Intact* with ATP produces a biphasic decrease in TMR fluorescence; this implies that NL movement occurs in two phases: NL docking when ATP binds followed by NL reorientation on hydrolysis (15). By contrast, mixing with ADP produces a monophasic fluorescence decrease (Fig. 4A). As expected, the amplitude of the fluorescence change is the same in both cases, since ATP hydrolysis and P_i release ultimately generate K5-ADP. The rate constants for both phases of the ATP transient vary hyperbolically with [ATP], defining maximum rate constants of 30.1 ± 2.0/s and 6.1 ± 0.6/s (Fig. 4A, left). The corresponding rate constant for the ADP transient also varies hyperbolically with [ADP], with an extrapolated rate constant of 11.9 ± 1.1/s (Fig. 4A, left). Analysis of the *NT Deleted* construct produced qualitatively similar results (Fig. 4A, right) where ATP binding also produced a biphasic fluorescence decrease, and the rate constants for both phases also varied with [ATP], defining maximum extrapolated rates of 13.1 ± 0.9 and 4.5 ± 0.4/s. However, while the rate constant for the slower phase with the *NT Deleted* construct is minimally different, that for the faster phase is nearly 130% lower than for *NT Intact*. In the case of the ADP transient (Fig. 4A, right), the rate constant also varies hyperbolically with [ADP], defining a maximum rate of 8.5 ± 0.3/s. These data demonstrate that the K5 N-terminus assists ATP-dependent NL movement, such that its deletion perturbs NL structural transitions and presumably force production.

To directly assess motor functionality, we compared the activity of the *NT Intact* and *NT Deleted* constructs in an *in vitro* MT gliding assay (Fig. 4B; Movies S3

and S4). Using automated MT tracking (see SI text and Fig. S7), our data show that the tracks for the *NT Deleted* construct are qualitatively similar to those for the *NT Intact* construct, but their average speed is slower (25.7 nm/s *NT Intact* compared to 17.4 nm/s *NT Deleted*, $p<0.001$) (Fig. 4B), consistent with rates measured for this construct in the steady-state ATPase assay (Fig. S6). Thus, the K5 N-terminus is required to kinetically assist NL docking and reorientation and hence to ensure efficient force generation and motility.

Molecular adaptations of kinesin MDs: model of coordination between NL and N-terminus for K5 force generation and motility. The comprehensive visualisation of the mechanochemical cycle of the MT-bound human K5 described here reveals remarkable plasticity within the MD and highlights important molecular adaptations of kinesin motors. Particularly, our data reveal the extent of conformational coordination between the NL and N-terminus that contributes to K5 function (Fig. 5). The NL and N-terminus form the CNB in MT-bound ATP state (13-16) and our current work now reveals the surprisingly transient nature of the CNB during the K5 ATPase cycle. As ATP hydrolysis is initiated, subtle, coupled conformational changes of the NL and N-terminus occur: the CNB partially melts thereby destabilising the plus-end directed conformation of the NL (Fig. 5, step A). This shows that throughout the ATPase cycle, NL movement can be controlled not only by the large-scale seesaw motion of the entire MD (15, 29), but also by more subtle destabilisation of the CNB. The N-terminus is structurally linked to the active site by helix $\alpha 0$, suggesting the allosteric route by which the nucleotide state of the K5 MD is communicated to the N-terminus. Hence, our ADP.AlFx reconstruction – supported by our biophysical measurements - provides the first direct evidence that the N-terminus plays a key role in K5 mechanochemistry, not only by assisting NL docking for force generation (Fig. 5, step D), but also by inducing its gradual undocking as the ATPase cycle proceeds.

NL reorientation towards the MT minus-end is completed in solution following phosphate release and MT detachment (Fig. 5, step B). Following NL reorientation and MT re-binding, the K5 N-terminus appears quite stable and could block reversion of the NL towards the MT plus-end. This stabilisation of the K5 N-terminus could also be part of the trigger that stimulates ADP release. MT-stimulated ADP release results in tilting of the MD towards the MT to form a high affinity nucleotide-free complex (Fig. 5, step C). In this rigor state, the NL conformation is more clearly visualised compared to the ADP state but remains directed towards the MT minus end. On the other hand, the K5 N-terminus is flexible and, thus, is less well defined in our rigor

reconstruction. However, our biophysical analyses of the K5 mutant lacking the N-terminus demonstrate that on ATP binding and the accompanying seesawing of the MD (Fig. 5, step D), the N-terminus is important for the efficient NL docking that powers K5 motility. In this state, the CNB is reformed with both the NL and N-terminus pointing towards the MT plus end. In summary, the interdependence of NL and N-terminus movement and flexibility seen in our reconstructions emphasizes the important regulatory role played by the long K5-specific N-terminus for force generation: it assists NL docking when ATP binds (Fig. 5, step D), triggers NL undocking on ATP hydrolysis (Fig. 5, step A) and physically limits search space of the flexible NL in the ADP state ensuring its minus-end directed conformation (Fig. 5, step B). These movements appear to be controlled, at least in part, by the relay of information from the active site by helix α0. Thus, the NL undergoes a large ordered movement back and forth along the K5 MD during one ATPase cycle orchestrated by lower amplitude movement of the N-terminus (Fig. 5, compare steps A and D).

CONCLUSION

Previous subnanometer resolution cryo-EM reconstructions of the MT-bound K1 MD led to the seesaw model of plus-end directed kinesin mechanochemistry (24), and K1s were the first family in which the importance of CNB formation for force generation was characterised (13, 14). The seesaw-related conformational changes we observe in the K5 MD at the ADP.AlFx to ADP transition - as well as rigor to AMPPNP - are likely to be shared by all plus-end directed kinesins (29). However, the other conformational changes we have visualised - rolling of the K5 MD, unfurling of L5 and the coordinated motions of the NL and N-terminus - are K5-specific. Although the flexibility of the K5 NL varies in different nucleotide states, we have directly visualised its orientation throughout the motor's ATPase cycle. In contrast, the shorter K1 NL is more flexible, and thus not visualised in rigor and ADP states (24, 30) implying intrinsic differences in the mechanical properties of K1 and K5 NLs (Fig. 5). This idea is further supported by our data showing that, even when K5 CNB formation is not possible in our *NT deleted* mutant, NL docking and motility are observed, albeit less efficiently compared to the *NT intact* MD (Fig. 4). Globally, K1 and K5 mechanochemistries share conserved nucleotide binding motifs, large seesaw movements and CNB formation. Recent studies are also converging to the conclusion that K1 and K5 have similar processivities (31). However, many other aspects of their enzymologies and molecular mechanisms are very different: the K1 N-terminus is required for force generation, whereas our data suggest that the K5 N-terminus plays a regulatory role at multiple steps throughout the motor's ATPase

cycle. Disruption of the CNB as soon as ATP hydrolysis occurs might destabilise K5 dimeric motors on the MT track, which could explain their sensitivity to load compared to K1 (11). The K5 N-terminus could interact with the C-terminus of the full-length protein in the context of the K5 tetramer to control stepping (32) and could also be subject to cell cycle-dependent regulation (Fig. S8). Additional differences elsewhere in the MDs – for example in L5 - are allosterically amplified to produce motors with very different mechanical outputs. Drug binding to the K5 L5 likely indirectly blocks movement elsewhere in the MD and hence the motor's ATPase and directional motility.

Molecular adaptations within the kinesin MD such as those highlighted in our study indicate that the properties of an individual motor cannot be directly extrapolated from those of the so-called paradigm K1. Such adaptations are likely to operate across the whole superfamily to support functional divergence. Future work will be directed towards elucidation of the molecular contribution of these divergent regions of kinesins in diverse functional settings.

MATERIALS AND METHODS

Sample preparation for cryo-EM and kinetics/biophysical experiments was performed as described previously (8, 15, 17). Full details of our methods for 3D reconstructions (24, 33) and for atomic model building are provided in SI Text. Reconstructions will be deposited in the EMDB, along with docked coordinates, on acceptance for publication. The kinetics of NL movement was measured as previously described (15) using TMR-labelled MD complexes. The gliding assay (34) was done in a flow cell in which K5 constructs were attached via penta-His antibodies. Motion of the fluorescent, rhodamine-labelled MTs (Cytoskeleton Inc.) was monitored using an inverted microscope (Nikon, TE2000). Additional details may be found in SI Text.

Acknowledgments

The authors thank Charles Sindelar (Yale University, USA) for reconstruction algorithms and Maya Topf, Elena Orlova and other members of the Birkbeck EM group for helpful discussions, Dr Dan Safer for undecagold and the BBSRC (BB/H005137/1) and NIH (GM102875-07 (to SR), GM64624 (to SPG)) for funding.

Author contributions

AG, SG, SSR and CAM designed the experiments. AG, JM, YJ and SSR performed the experiments. AG, YJ, SG, SSR and CAM analysed the data and wrote the paper.

Conflict of interest

The authors declare that they have no conflict of interest.

REFERENCES

1. Hirokawa N, Noda Y, Tanaka Y, & Niwa S (2009) Kinesin superfamily motor proteins and intracellular transport. *Nat Rev Mol Cell Biol* 10(10):682-696.
2. Vale RD & Milligan RA (2000) The way things move: looking under the hood of molecular motor proteins. *Science* 288(5463):88-95.
3. Goulet A & Moores C (2013) New insights into the mechanism of force generation by Kinesin-5 molecular motors. *International review of cell and molecular biology* 304:419-466.
4. Acar S*, et al.* (2013) The bipolar assembly domain of the mitotic motor kinesin-5. *Nat Commun* 4:1343.
5. Kapitein LC*, et al.* (2005) The bipolar mitotic kinesin Eg5 moves on both microtubules that it crosslinks. *Nature* 435(7038):114-118.
6. Cahu J & Surrey T (2009) Motile microtubule crosslinkers require distinct dynamic properties for correct functioning during spindle organization in Xenopus egg extract. *J Cell Sci* 122(Pt 9):1295-1300.
7. Cochran JC*, et al.* (2004) Mechanistic analysis of the mitotic kinesin Eg5. *J Biol Chem* 279(37):38861-38870.
8. Rosenfeld SS, Xing J, Jefferson GM, & King PH (2005) Docking and rolling, a model of how the mitotic motor Eg5 works. *J Biol Chem* 280(42):35684-35695.
9. Cross RA (2004) The kinetic mechanism of kinesin. *Trends in biochemical sciences* 29(6):301-309.
10. Cochran JC, Krzysiak TC, & Gilbert SP (2006) Pathway of ATP hydrolysis by monomeric kinesin Eg5. *Biochemistry* 45(40):12334-12344.
11. Valentine MT, Fordyce PM, Krzysiak TC, Gilbert SP, & Block SM (2006) Individual dimers of the mitotic kinesin motor Eg5 step processively and support substantial loads in vitro. *Nat Cell Biol* 8(5):470-476.
12. Block SM, Asbury CL, Shaevitz JW, & Lang MJ (2003) Probing the kinesin reaction cycle with a 2D optical force clamp. *Proc Natl Acad Sci U S A* 100(5):2351-2356.
13. Hwang W, Lang MJ, & Karplus M (2008) Force generation in kinesin hinges on cover-neck bundle formation. *Structure* 16(1):62-71.
14. Khalil AS*, et al.* (2008) Kinesin's cover-neck bundle folds forward to generate force. *Proc Natl Acad Sci U S A* 105(49):19247-19252.
15. Goulet A*, et al.* (2012) The Structural Basis of Force Generation by the Mitotic Motor Kinesin-5. *J Biol Chem*. 285(53):44654-44666.
16. Hesse WR*, et al.* (2013) Modular aspects of Kinesin force generation machinery. *Biophys J* 104(9):1969-1978.
17. Behnke-Parks WM*, et al.* (2011) Loop L5 acts as a conformational latch in the mitotic kinesin Eg5. *J Biol Chem* 286(7):5242-5253.
18. Waitzman JS*, et al.* (2011) The loop 5 element structurally and kinetically coordinates dimers of the human kinesin-5, Eg5. *Biophys J* 101(11):2760-2769.
19. Larson AG, Naber N, Cooke R, Pate E, & Rice SE (2010) The conserved L5 loop establishes the pre-powerstroke conformation of the Kinesin-5 motor, eg5. *Biophys J* 98(11):2619-2627.
20. Cochran JC, Gatial JE, 3rd, Kapoor TM, & Gilbert SP (2005) Monastrol inhibition of the mitotic kinesin Eg5. *J Biol Chem* 280(13):12658-12667.
21. Kwok BH*, et al.* (2006) Allosteric inhibition of kinesin-5 modulates its processive directional motility. *Nat Chem Biol* 2(9):480-485.
22. Mayer TU*, et al.* (1999) Small molecule inhibitor of mitotic spindle bipolarity identified in a phenotype-based screen. *Science* 286(5441):971-974.

23. Rosenfeld SS, Rener B, Correia JJ, Mayo MS, & Cheung HC (1996) Equilibrium studies of kinesin-nucleotide intermediates. *J Biol Chem* 271(16):9473-9482.
24. Sindelar CV & Downing KH (2010) An atomic-level mechanism for activation of the kinesin molecular motors. *Proc Natl Acad Sci U S A* 107(9):4111-4116.
25. Parke CL, Wojcik EJ, Kim S, & Worthylake DK (2010) ATP hydrolysis in Eg5 kinesin involves a catalytic two-water mechanism. *J Biol Chem* 285(8):5859-5867.
26. Turner J*, et al.* (2001) Crystal structure of the mitotic spindle kinesin Eg5 reveals a novel conformation of the neck-linker. *J Biol Chem* 276(27):25496-25502.
27. Kull FJ & Endow SA (2013) Force generation by kinesin and myosin cytoskeletal motor proteins. *Journal of cell science* 126(1):9-19.
28. Kim ED*, et al.* (2010) Allosteric drug discrimination is coupled to mechanochemical changes in the kinesin-5 motor core. *J Biol Chem* 285(24):18650-18661.
29. Sindelar CV (2011) A seesaw model for intermolecular gating in the kinesin motor protein. *Biophys Rev* 3(2):85-100.
30. Rice S*, et al.* (1999) A structural change in the kinesin motor protein that drives motility. *Nature* 402(6763):778-784.
31. Shastry S & Hancock WO (2011) Interhead tension determines processivity across diverse N-terminal kinesins. *Proc Natl Acad Sci U S A* 10839):16253-16258.
32. Weinger JS, Qiu M, Yang G, & Kapoor TM (2011) A nonmotor microtubule binding site in kinesin-5 is required for filament crosslinking and sliding. *Curr Biol* 21(2):154-160.
33. Sindelar CV & Downing KH (2007) The beginning of kinesin's force-generating cycle visualized at 9-A resolution. *J Cell Biol* 177(3):377-385.
34. Leduc C, Ruhnow F, Howard J, & Diez S (2007) Detection of fractional steps in cargo movement by the collective operation of kinesin-1 motors. *Proc Natl Acad Sci U S A* 104(26):10847-10852.

FIGURES LEGENDS

Figure 1. The ATP hydrolysis transition state: MD tilting, L5 uncurling and cover–neck bundle destabilization. (A) MT-bound K5 MD in the ADP.AlFx state (light blue surface, 1.1σ contour) with gold difference maps superimposed (blue (2.3σ), pink (2.2σ) and red (2.2σ) contours). The MT plus-end is towards the top of all figures. **(B)** Pseudo-atomic models of K5 MD (color-coded as in the key) bound to an αβ-tubulin dimer (green ribbon) docked into the reconstruction (contour as in (A), mesh: 3.3σ contour, ~1/3 of the volume). Residues to which gold clusters were covalently attached, and the nucleotide analogue are shown in space-filling representation. NL conformers clustered into docked (red) and disconnected (orange) conformations are indicated (SI Text). **(C,D)** View towards the nucleotide-binding pocket of the AMPPNP (15) (C: coral surface 1σ contour, mesh 3σ contour, to depict the same molecular volumes as in (B)) and ADP.AlFx (D: contoured as in (B))). The blue arrow indicates the absence of contact between helix α0 and switch I in the ADP.AlFx state, which is present in the AMPPNP state. **(E)** Comparison of K5 MD models of ADP.AlFx (colored as in the key) and AMPPNP states (coral (15)), superimposed on helices α4. ATP hydrolysis triggers a tilt of the MD towards the MT lattice (colored arrow). L5 uncurls from its arch-like conformation upon ATP hydrolysis (comparison based on superimposed helices α2). Displacements of helix α3/switch I and helix α0 are due to MD tilting.

Figure 2. The ADP, MT weak-binding state. (A) ADP state (1.5σ contour, the same volume as in Fig. 1A) with gold density difference maps superimposed (blue (1.5σ), pink (2.5σ) and red (1.9σ) contours). **(B)** Pseudo-atomic model of K5 MD bound to an αβ-tubulin dimer (surface contoured as in (A), mesh 3σ contour (1/3 of the surface volume)). The red arrow indicates the absence of EM density accommodating the N-terminal part of the NL and the C-terminal part of helix α6 to which it is attached. **(C,D)** Comparison of K5 MD pseudo-atomic models of the ADP.AlFx (C) and ADP (D) states; surfaces and meshes are contoured as in Fig. 1C (C, ADP.AlFx) and Fig. 2B (D, ADP). The yellow arrow indicates the lack of density for switch II that is therefore absent in our ADP model. **(E)** The ADP MT-weakly bound state is rotated clockwise with respect to the MT axis compared to the ADP.AlFx state (color-coded arrows). The surface is contoured at 2σ and only some of the secondary structural elements are shown for clarity.

Figure 3. Conformational changes associated with ADP release. (A,B) K5 MD pseudo-atomic models of the ADP (light purple) and rigor states are superimposed on helices α4 and docked into the rigor reconstruction (15); surface (0.94σ contour) and mesh (3σ contour). **(A)** The position of the gold density (blue surface, 1.4σ contour) attached to the N-terminus via A9C - at ~ 23Å or ~7 amino acids away from the first residue in our rigor model (G16) - confirms our previous assignment of the N-terminus in the rigor reconstruction (15). The color-coded arrow indicates the direction of the MD tilt around the helix α4 and towards the MT lattice upon ADP release. **(B)** Upon ADP release, L5 moves towards the empty nucleotide-binding pocket, based on superimposition of helices α2. The black arrowhead and the blue arrow indicate a connection between L5 and switch I (SI) and between L5 and helix α0, respectively. Helix α3/switch I, helix α4 and helix α0 of the ADP model are also shown for comparison.

Figure 4. Effect of deletion of the K5 N-terminus on kinetic parameters and motility. (A) The jagged curves represent the observed fluorescence transient, by mixing TMR-labelled *NT Intact:*MT (left) and TMR-labelled *NT Deleted:*MT (right) complex with 800 μM ATP or ADP, and the smooth curves are fit to a double (red) or single (blue) exponential rate equation. Insets: Plot of rate constant *versus* [ATP] or [ADP]. **(B)** Individual MT gliding traces for *NT Intact* (blue) and *NT Deleted* (red) constructs. Each set of traces (N= 17 and 22, respectively) were averaged together pointwise to extract average behavior (blue (25.7 nm/sec) and red (17.4 nm/sec)) traces with error bars, which are SEM); individual frames were 85 ms apart (see SI text).

Figure 5. Molecular adaptations of kinesin motors: N-terminus/NL conformational coupling during the mechanochemical cycle. The central schematic illustrates the MT-based ATPase cycle: ATP hydrolysis (A), Pi release/MT detachment and MT re-binding (B), ADP release (C) and ATP binding (D). Around this are depicted the major nucleotide-dependent conformational changes in the K5 N-terminus and NL. The large seesawing motion of the MD at steps B and D is shown by rotation of the K5 MD on the αβ-tubulin dimer. The proposed route of structural communication between helix α0 proximal to the active site via strand β1 is shown. Stability of the N-terminus/NL is depicted as a solid line, while flexibility is indicated by a dotted line. CNB formation is indicated by a black square. The outer cycle depicts the conformational changes in the K1 MD (24, 30). In contrast to K5

however, both the K1 N-terminus and NL are highly flexible in both the ADP and rigor states. The exact route of structural communication between the K1 helix $\alpha 0$ and N-terminus has not been described.

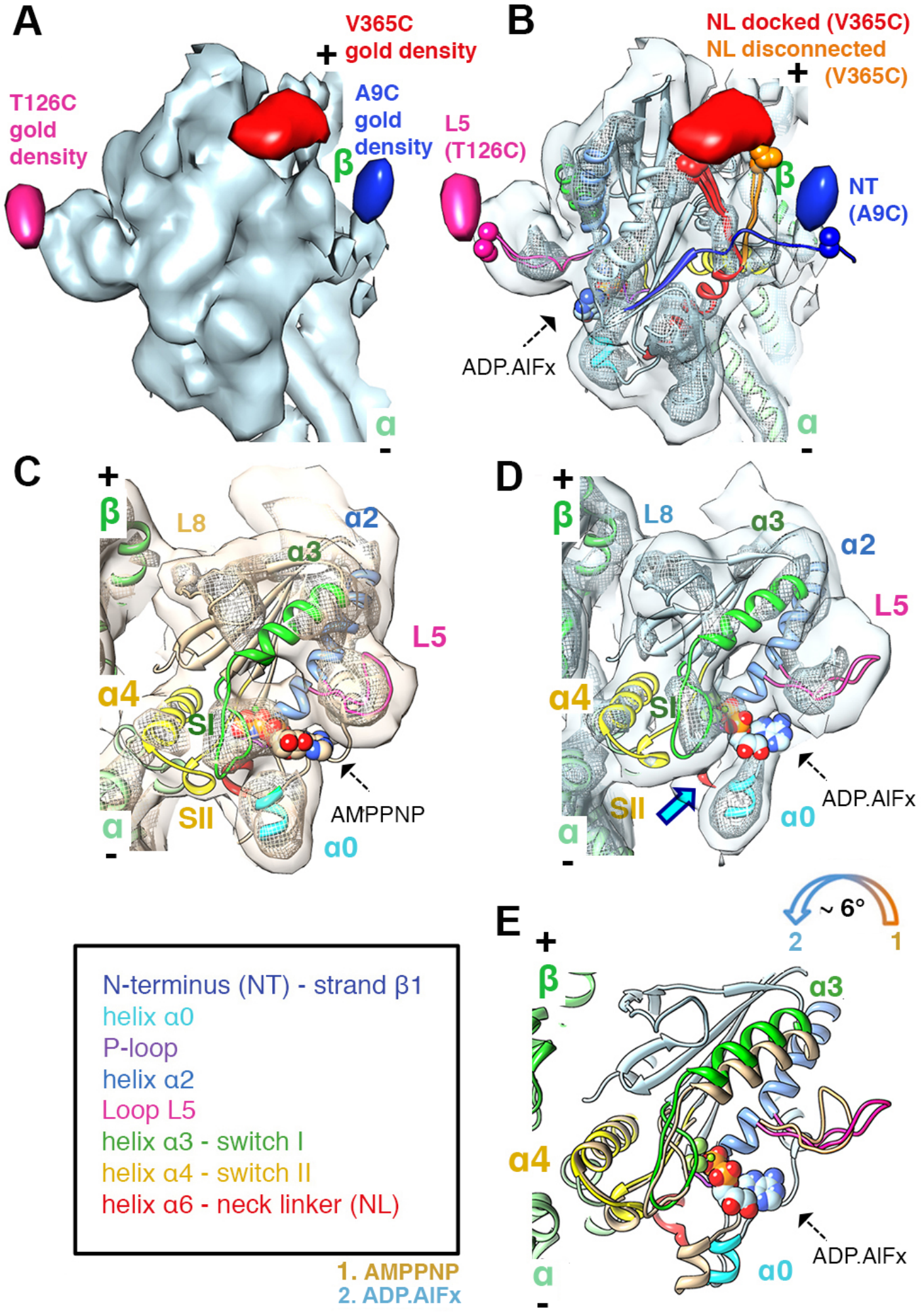
A
V365C
gold density
+
T126C
gold
density
A9C
gold
density
β
α
-
B
NL docked (V365C)
NL disconnected
(V365C)
+
L5
(T126C)
β
NT
(A9C)
ADP.AlFx
α
-
C
+
β
L8
α2
α3
L5
α4
SI
SII
AMPPNP
α
-
α0
D
+
β
L8
α3
α2
L5
α4
SI
SII
ADP.AlFx
α0
α
-
E
~ 6°
2
1
+
β
α3
α4
ADP.AlFx
α0
α
-
N-terminus (NT) - strand β1
helix α0
P-loop
helix α2
Loop L5
helix α3 - switch I
helix α4 - switch II
helix α6 - neck linker (NL)
1. AMPPNP
2. ADP.AlFx

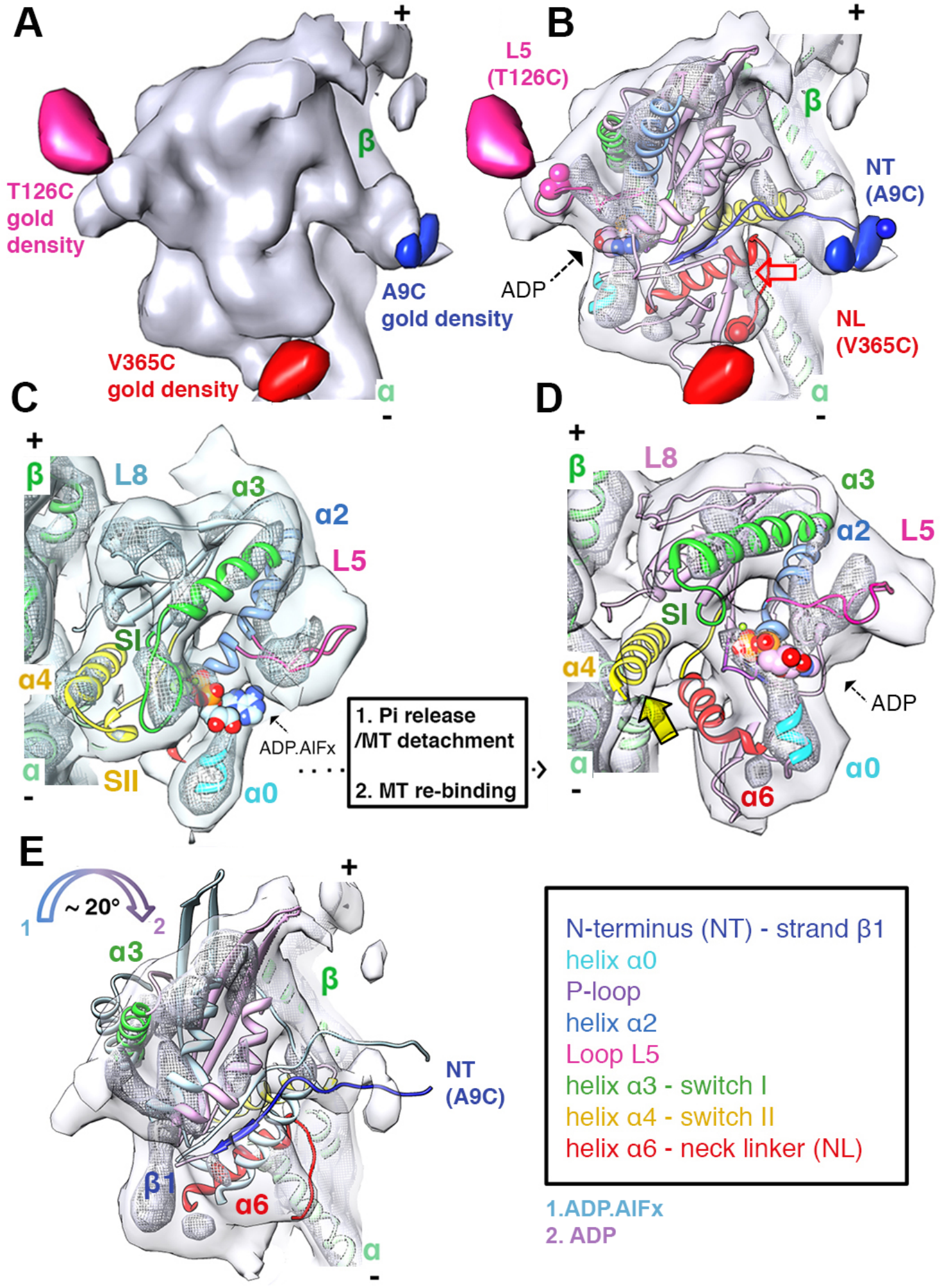
A
+
β
T126C
gold
density
A9C
gold density
V365C
gold density
α
-
B
+
L5
(T126C)
β
NT
(A9C)
ADP
NL
(V365C)
α
-
C
+
β
L8
α3
α2
L5
SI
α4
ADP.AIFx
α
SII
α0
-
1. Pi release
/MT detachment
2. MT re-binding
D
+
β
L8
α3
α2
L5
SI
α4
ADP
α
α0
α6
-
E
~ 20°
1
2
+
α3
β
NT
(A9C)
β1
α6
α
-
N-terminus (NT) - strand β1
helix α0
P-loop
helix α2
Loop L5
helix α3 - switch I
helix α4 - switch II
helix α6 - neck linker (NL)
1.ADP.AIFx
2. ADP

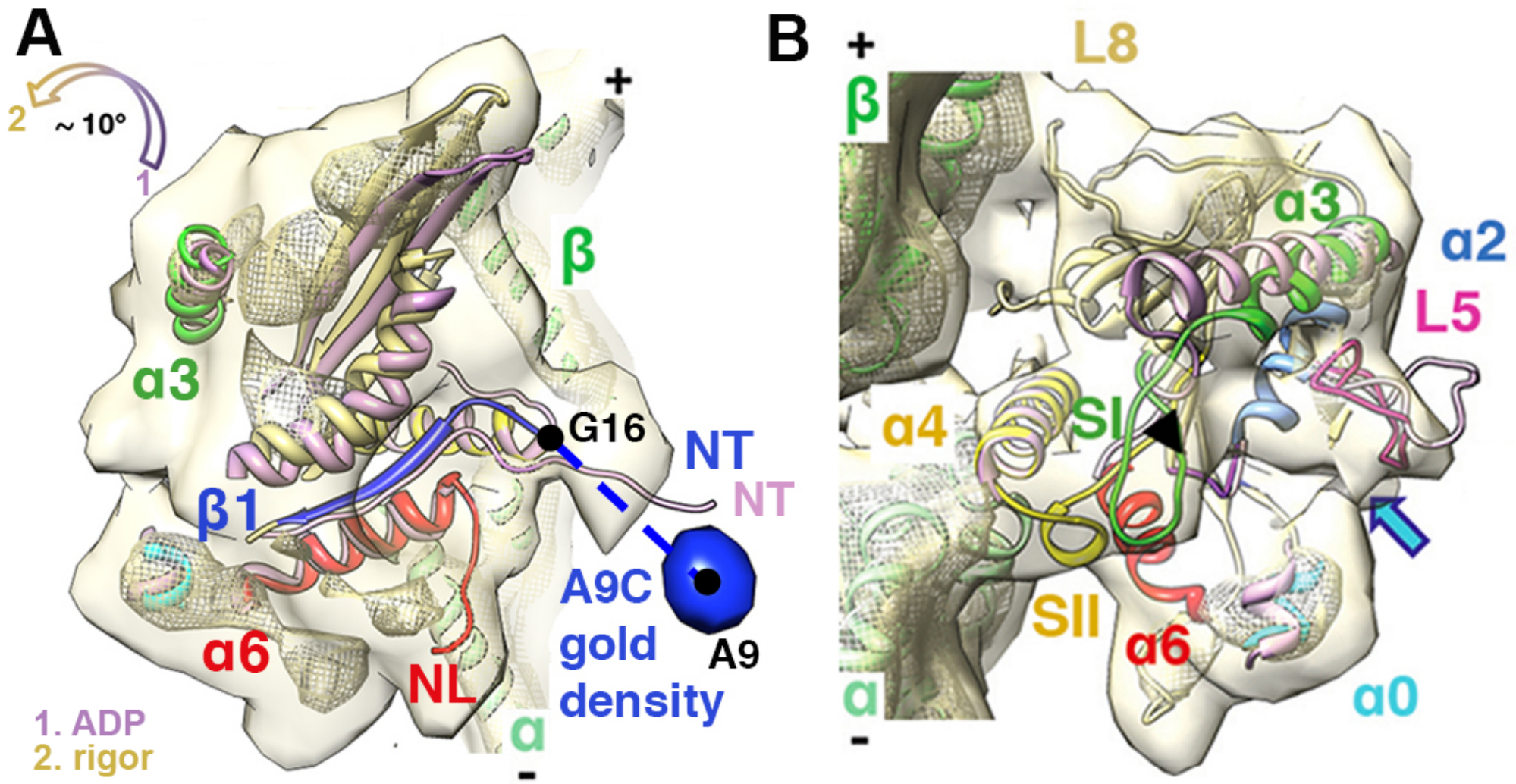
A
2
~10°
1
+
β
α3
G16
NT
NT
β1
A9C
gold
density
A9
α6
NL
α
-
1. ADP
2. rigor
B
+
L8
β
α3
α2
L5
α4
SI
SII
α6
α0
α
-

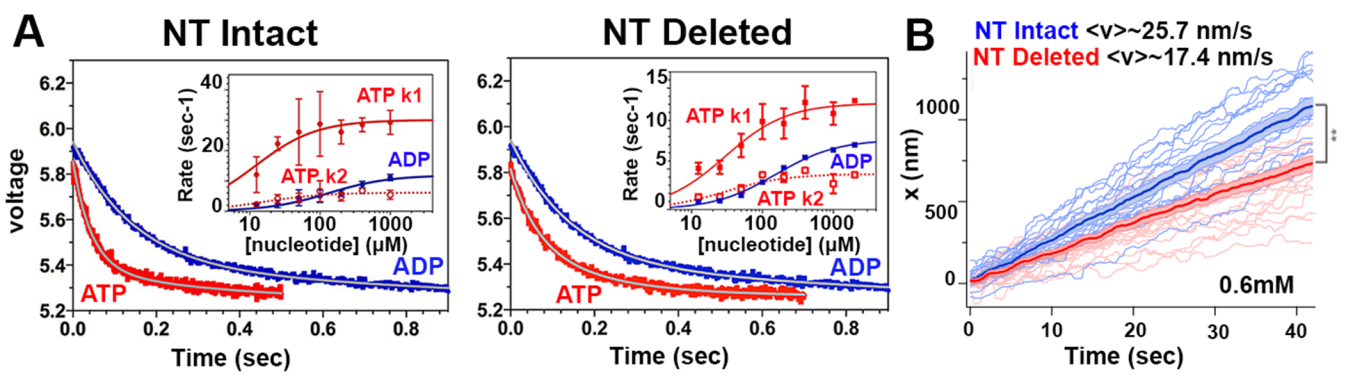
A
NT Intact
NT Deleted
voltage
Time (sec)
ATP
ADP
ATP k1
ATP k2
Rate (sec-1)
[nucleotide] (μM)
B
NT Intact <v>~25.7 nm/s
NT Deleted <v>~17.4 nm/s
x (nm)
Time (sec)
0.6mM
**

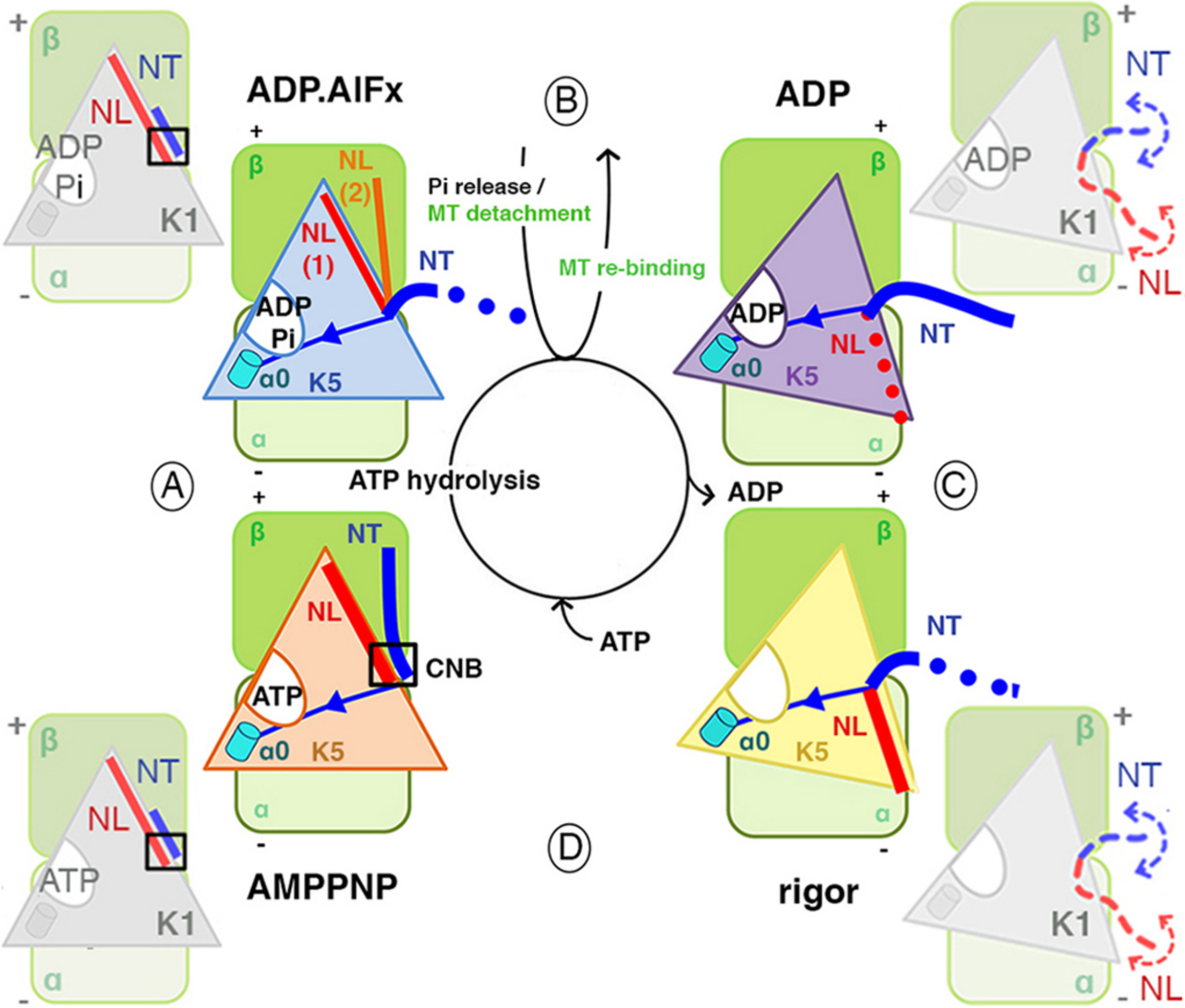
ADP.AlFx
B
ADP
Pi release /
MT detachment
MT re-binding
NL
(2)
NL
(1)
NT
ADP
Pi
α0
K5
β
α
+
-
A
ATP hydrolysis
ADP
C
ATP
CNB
AMPPNP
D
rigor
K1

SUPPLEMENTARY INFORMATION

SUPPLEMENTARY METHODS

Production and labelling of K5 constructs

Cysteine-light human K5 MD constructs (residues 1-367) with a single cysteine on L5 (T126C) or on the NL (V365C) were recombinantly expressed in *E. coli* and purified using a C-terminal His_6-tag as previously described (1-3). We also generated a construct containing a cysteine in the N-terminus (A9C) by chemical synthesis (GenScript, Piscataway, NJ), cloned into a pET21a expression vector. An undecagold cluster conjugated to a maleimide linker, provided by Dr Dan Safer (University of Pennsylvania, USA), was used to covalently label single cysteines in the K5 constructs T126C, V365C and A9C. Protocols for gold and protein activation and labelling of T126C and V365C were previously reported (3). The A9C K5 construct was exchanged into labelling buffer (10 mM Hepes pH 7, 25 mM K-acetate, 1 mM Mg-acetate, 1 mM EGTA) supplemented with 1 mM TCEP (Sigma) using a PD10 desalting column (Amersham Biosciences). Eluted protein was incubated for 45 min at room temperature with 5U/mL apyrase to remove bound nucleotides, and recovered by nickel affinity chromatography. Immediately prior to mixing with a 40-fold molar excess of activated gold, the nucleotide-free A9C K5 construct was exchanged into labelling buffer without TCEP. After 18 hours incubation at room temperature, labelled A9C proteins were recovered by nickel affinity chromatography. The labelling efficiency given by the concentrations of eluted protein and attached gold (determined by absorbance at 420 nm) was 64%.

We also generated two additional K5 MD constructs to monitor NL movement and the effect of deleting the N-terminus on this process. The first, described previously (3), consists of a 1-367 monomeric construct containing two cysteines at positions 365 and 256 (V256C, V365C). We previously showed that these mutations do not have any appreciable effect on the MT-activated ATPase k_{cat}. We also demonstrated in that study that attaching distance sensitive fluorescent probes at these locations allows us to monitor the kinetics of nucleotide induced NL movement, since the cysteine at position 256 is likely to serve as a stable frame of reference. In this current study, we refer to this construct as *NT Intact.* The other construct is equivalent to the NT Intact construct, except that the first 17 amino terminal residues have been deleted. We refer to this construct as *NT Deleted*. Both constructs were generated from inserts that were chemically synthesized (GenScript) and cloned into pET21a. Both constructs were labelled with tetramethyl rhodamine 5' maleimide

(TMR) by incubation for 24 hours with a 10-fold molar excess of TMR over MD, followed by gel filtration on Sephadex G25 to remove unbound label. Labelling stoichiometries of 1.7-1.9 were achieved for both constructs.

Cryo-EM image analysis

Bovine brain tubulin (Cytoskeleton, Inc.), at a final concentration of 5mg/ml, was incubated for 1H30 at 37°C in a buffer containing 100mM MES pH 6.5, 1mM $MgCl_2$, 1mM EGTA, 1mM DTT and 2mM GTP. Polymerized MTs were stabilized with 1mM Paclitaxel (Calbiochem) in dimethyl sulfoxide for a further 1H30 at 37°C. K5 MD was dialysed into 80mM PIPES pH 6.8, 5mM $MgCl_2$, 1mM EGTA 1mM TCEP before incubation with ADP aluminium fluoride, or into 20mM PIPES pH 6.8, 5mM $MgCl_2$, 1mM EGTA, 1mM TCEP before incubation with ADP. MTs (2µM) were incubated at room temperature with either 1) a 10-fold molar excess of K5 MD (20µM) and 2mM ADP/ 2mM $AlCl_3$/ 7mM NaF for 45min, or 2) with a 15-fold excess of K5 MD (30µM), pre-incubated for 5 min on ice with 10mM ADP and 2.5% w/v glycerol for ≈ 30 sec. Subsequently, 3.5µl of the MT-MD mixture was applied to glow-discharged C-flat holey carbon grids (Protochips Inc.) at 24°C and 100 % humidity, and automatically blotted and plunged into liquid ethane (Vitrobot, FEI Company). Low dose images were acquired using a Tecnai F20 FEG microscope (FEI Company) operating at 200 kV using a Gatan CT3500 Cryotransfer System (Gatan, Inc.). Micrographs were recorded at 0.7-2.4µm defocus, 50,000x nominal magnification on Kodak SO-163 films digitized (SCAI scanner: Carl Zeiss, Inc) to a final sampling of 1.4Å/pixel (ADP.AlFx) or at 68,000x magnification on a 4k x 4k CCD camera (Gatan) with a sampling of 2.2Å/pixel (ADP).

Three-dimensional reconstructions were produced using a previously described custom single particle procedure (4, 5), which combines manual particle picking using Boxer (6), angle determination by projection matching using SPIDER (7), and angle refinement, 3D reconstruction and full CTF correction using FREALIGN (8). 139,000 and 125,000 asymmetric units (MD bound to an αβ-tubulin dimer) boxed from 167 and 213 13-protofilaments MTs gave an isotropic angular distribution (Table S1, Fig. S1) and were used to calculate the 3D reconstructions of the ADP.AlFx and ADP states respectively. The resolution of the ADP.AlFx and ADP reconstructions were estimated at 9.2Å and 10Å respectively using the Fourier Shell Correlation 0.5 criterion. The occupancy of the disconnected NL EM density in the ADP.AlFx reconstruction was calculated from the ratio between the mean voxel values of this density and of a section of similar volume in the body of the MD (the

helix α4 region). Asymmetric units of the ADP.AlFx and ADP reconstructions will be deposited in the EMDB on acceptance for publication.

The same reconstruction procedure was applied to the gold-labelled T126C (T126C-Au), V365C (V365C-Au) and A9C (A9C-Au). The presence of the gold cluster did not perturb the overall structure of K5 MDs and gold densities were readily visible (Fig. S2). To extract gold-specific densities, difference maps were calculated between scaled and aligned gold-labelled and unlabelled reconstructions in each nucleotide state, each band-pass filtered at the same frequencies, using SPIDER (7) and IMAGIC-5 (9). An asymmetric unit of each of these maps will also be deposited in the EMDB. We also prepared cryo-EM samples of the AMPPNP and rigor states using gold-labelled A9C following the procedure described in (3). 3D reconstructions and difference maps were calculated as described above. An asymmetric unit of each of these maps will also be deposited in the EMDB.

Atomic model building

The coordinates of αβ-tubulin dimer (PDB 1JFF (10)) and of different conformations of human K5 MDs available in the PDB were rigidly fit into an asymmetric unit of the ADP.AlFx and ADP reconstructions using UCSF Chimera (11). The K5 MD coordinates with AMPPNP or ADP bound produced the highest cross-correlation value between the experimental and the model-based simulated maps and were used as starting model for the ADP.AlFx and ADP states respectively (Table S2). However, to account for the fact that helix α4 is longer in our reconstruction than in the available ADP crystal structures, we modelled 7 helical turns of helix α4 (residues D279-E304), as observed in K5 AMPPNP crystal structure, and modelled it in all our other reconstructions. Although almost identical cross-correlation (CC) values are obtained for MD models with a long (0.791) or a short (0.793) helix α4, the longer version is more consistent overall with our reconstructions and with the observation of a long helix α4 of constant length in all four nucleotide states of K1 MD reconstructions (5). Due to the absence of well-defined density accounting for switch II loop in our ADP reconstruction, we did not model residues N271-K280, which are also missing in the available ADP crystal structures. The coordinates of αβ-tubulin/K5 MD complexes were refined by flexible fitting using Flex-EM (12). To avoid overfitting, the rigid bodies used in the first cycle of flexible fitting were defined using the server RIBFIND (13). In a second cycle, individual secondary structure elements were released.

After the overall conformation of the K5 MD in each nucleotide state was modelled, the conformations of the N-terminus, L5 and NL in the MD were more

precisely defined. These mechanochemical elements are either absent in the available K5 MD crystal structures or are in a conformation that does not match the EM density. Using Modeller (14, 15), we generated 500 conformers of the N-terminus for the ADP.AlFx (11 amino acids N6-G16) and the ADP (7 amino acids A9-K15) states. The conformers in which A9 satisfied the constraint of the gold position were selected and the final conformation depicted in both states is the one that gave the highest CC value. Similarly, the final conformation of L5 in between the two Pro residues P121 and P131 (N122-D130) was generated by Modeller and selected among 250 initial conformers according to the same criteria. Finally, the disconnected conformation of the NL in the ADP.AlFx state was calculated using a conjugate-gradient energy minimization approach implemented in Flex-EM; this was applied to the complete MD model with the NL docked along the MD in order to sample its conformational space independently of the EM reconstruction. Among 100 conformations of the NL, 44 were selected in which V365C satisfies the gold density position. Subsequent ranking of these models based on the CC value and RMSD clustering Cα cut-off of 0.35Å produced 4 clusters: the first cluster, whose the 31 members have the highest CC, represents the docked conformation, the second cluster encompasses 9 conformations that fit into the EM density of the undocked conformation, the third cluster is close to the second, and the last conformer lies between the docked and undocked conformations (Fig. S3). The final ADP.AlFx and ADP models, in which the L5 and N-terminus conformation cannot be further refined at the current resolution, were energetically minimized and their stereochemistry was checked. The increase of CC values calculated with the initial and final models assesses the quality of the fit (Table S2). The atomic models will be deposited in the Protein Data Bank on acceptance for publication.

Kinetic Methodologies

The MT-activated ATPase activities of the K5 constructs were determined by measuring phosphate production with a commercially available kit (EnzChek, Molecular Probes). Assays contained 25-50 nM MD and a minimum of a 5-fold molar excess of MTs (Fig. S6).

We measured the kinetics of NL movement and of the effect of N-terminal deletion on this by labelling the two cysteines in the *NT Intact* and *NT Deleted* constructs with TMR. We mixed TMR-labeled MD complexes with a 3-5-fold molar excess of MTs by adding the two components together in buffer containing 50 mM potassium acetate, 25 mM HEPES, 5 mM magnesium acetate, 1 mM EGTA, 1 mM DTT, pH 7.50, 0.2 U/ml Type VII apyrase (Sigma-Aldrich) and incubating at 20^{o}C for

20 minutes prior to initiating the experiment. These samples were then mixed in a KinTek SF-2004 stopped-flow spectrophotometer with an instrument dead time of 1.2 milliseconds. The TMR fluorophore was excited at 520 nm and the fluorescence emission was monitored at 90^{o} to the incident beam through a 590 nm long pass filter was used to monitor changes in TMR emission.

Gliding assay and image acquisition

The gliding assay was done in a flow cell (microscope slide plus hydrophobic coverslip, separated with the double-side tape). Initially, the flow cell was filled with penta-His antibodies (200µg/ml, Qiagen) at 20µg/ml (2.5ml antibody and 22.5ml PEM80); after a 10 minute absorption the surface was blocked for 10 minutes by adding a casein solution (5.55 mg/mL of casein in 35 mM PIPES, 5 mM MgSO4, 1mM EGTA, 0.5 mM EDTA). Next motors were added (in 80 mM Pipes pH 6.9, 50 mM CH3CO2K, 4 mM MgSO4, 1 mM DTT, 1 mM EGTA, 10 µM paclitaxel, 1 mg/ml casein), and incubated for 5min to bind the motors specifically to the antibodies by their His-tags. Finally, 1µl of fluorescent MTs (30% rhodamine-tubulin (Cytoskeleton Inc, # T331) and 70% non-fluorescent tubulin) was added in 50µl of motility buffer with 0.6mM (Fig. 4B) or 1mM ATP (Fig S7) and oxygen-scavenging system (250 µg/ml glucose oxidase, 30 µg/ml catalase, 4.5 mg /ml glucose).

Motion of the MTs was monitored using an inverted microscope (Nikon, TE2000) with 100x objective (NA=1.49). Fluorescence images were acquired at 11.8 FPS using an EMCCD camera (Quantem 512SC, Photometrics, 512x512 imaging pixels) and µ-Manager software; one pixel corresponded to 60nm. Movies were composed of 500 images. To track the fluorescent MTs, images were first processed with Matlab to remove shot noise and to enhance the visibility of MTs. Then, the intensity profile of the MT from each frame was determined using ImageJ. After smoothing the intensity profile first with a median filter (5 points) and then with a Loess filter, we determined the tip position of MT in each frame from where the intensity from median filter and Loess filter becomes same. This yielded an uncertainty of approximately 1 pixel in the location of the MT tip, which likely accounts for some of the 'waviness' apparent in the trajectories. Finally, we smoothed each trajectory with a median filter (20 points). In some trials, a fraction (~30%) of the *NT Deleted* (but not *NT Intact*) MTs were paused on the coverslip, but in others, only a few were paused in each group. Paused MTs and MTs exhibiting stop-and-go motion were excluded from the analysis (3 such *NT Deleted* traces were excluded from 25 overall) where individual trajectories were averaged together.

SUPPLEMENTARY TABLES

Table S1. The resolution and the numbers of asymmetric units included in each cryo- EM reconstruction.

Nucleotide state	K5 sample	n. of asymmetric units (n. of MTs)	Resolution (Å) FSC 0.5
ADP.AlFx	unlabelled	~139,000 (167)	9.2
	T126C-Au	~7,300 (10)	19
	V365C-Au	~13,000 (13)	16
	A9C-Au	~14,000 (20)	18
ADP	unlabelled	~125,000 (213)	10
	T126C-Au	~13,000 (26)	18
	V365C-Au	~30,000 (49)	20
	A9C-Au	~14,000 (27)	18
AMPPNP	A9C-Au	~21,000 (31)	25
rigor	A9C-Au	~18,000 (17)	18

Table S2. Correlation values between the experimental and simulated maps for each K5 MD atomic model.

Models	Correlation values	
	ADP.AlFx	ADP
Initial models		
αβ-tubulin (1JFF) +3HQD (AMPPNP)	0.654	0.764
αβ-tubulin (1JFF) +1II6 (ADP)	0.640	0.768
αβ-tubulin (1JFF) +2WOG (ADP+drug)	0.648	0.767
αβ-tubulin (1JFF) +1Q0B (ADP+drug)	0.642	0.767
Final models	0.673 (NL docked) 0.671 (NL undocked)	0.791

SUPPLEMENTARY FIGURES

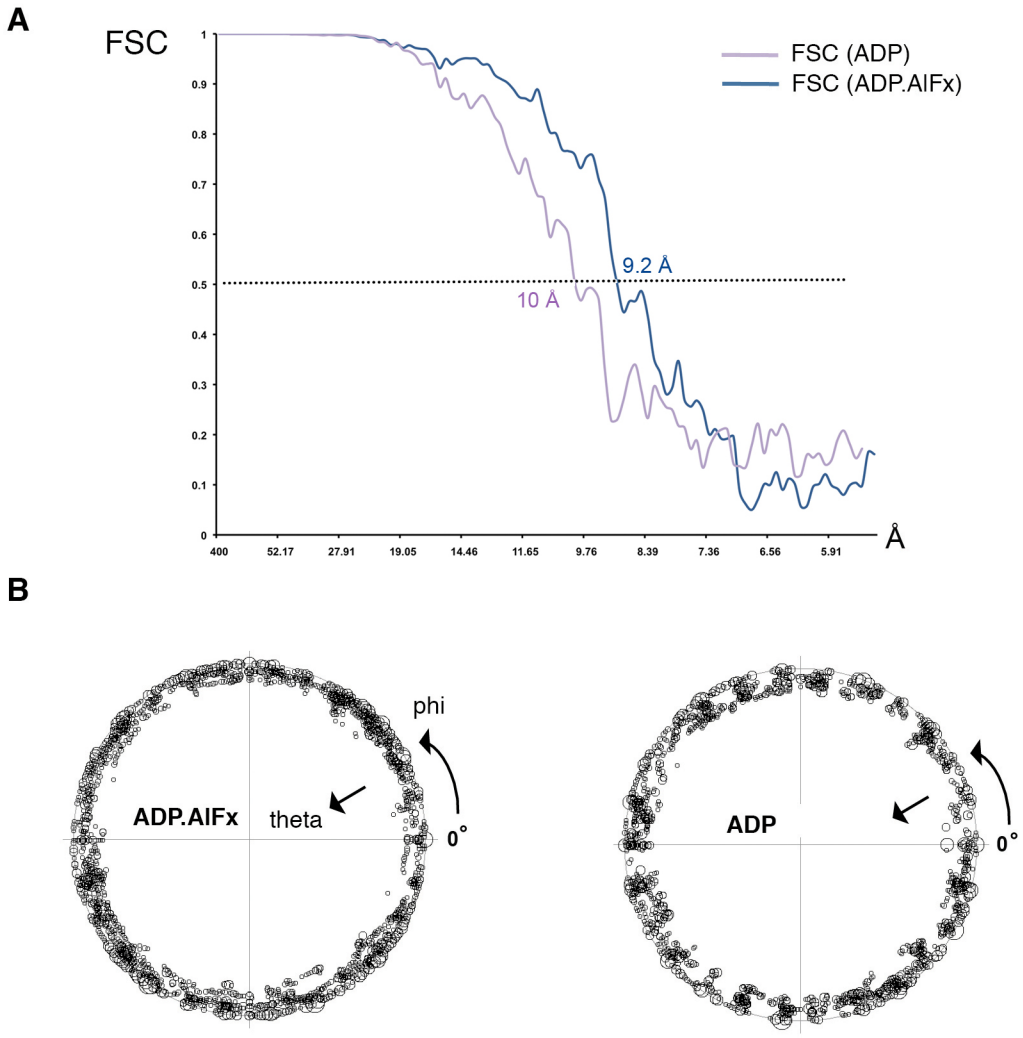

FIGURE S1. Resolution and data angular distribution of the cryo-EM reconstructions. (**A**) Fourier Shell Correlation (FSC) curves computed between two independent reconstructions for ADP.AlFx (blue) and ADP (purple) states. FSC 0.5 criterion indicates 9.2Å and 10Å resolution (dotted line). See also Table S1. (**B**) Angular distribution of the particles used for the ADP.AlFx and ADP reconstructions. The size of the small circles representing phi and theta angles is proportional to numbers of particle projections at that angle.

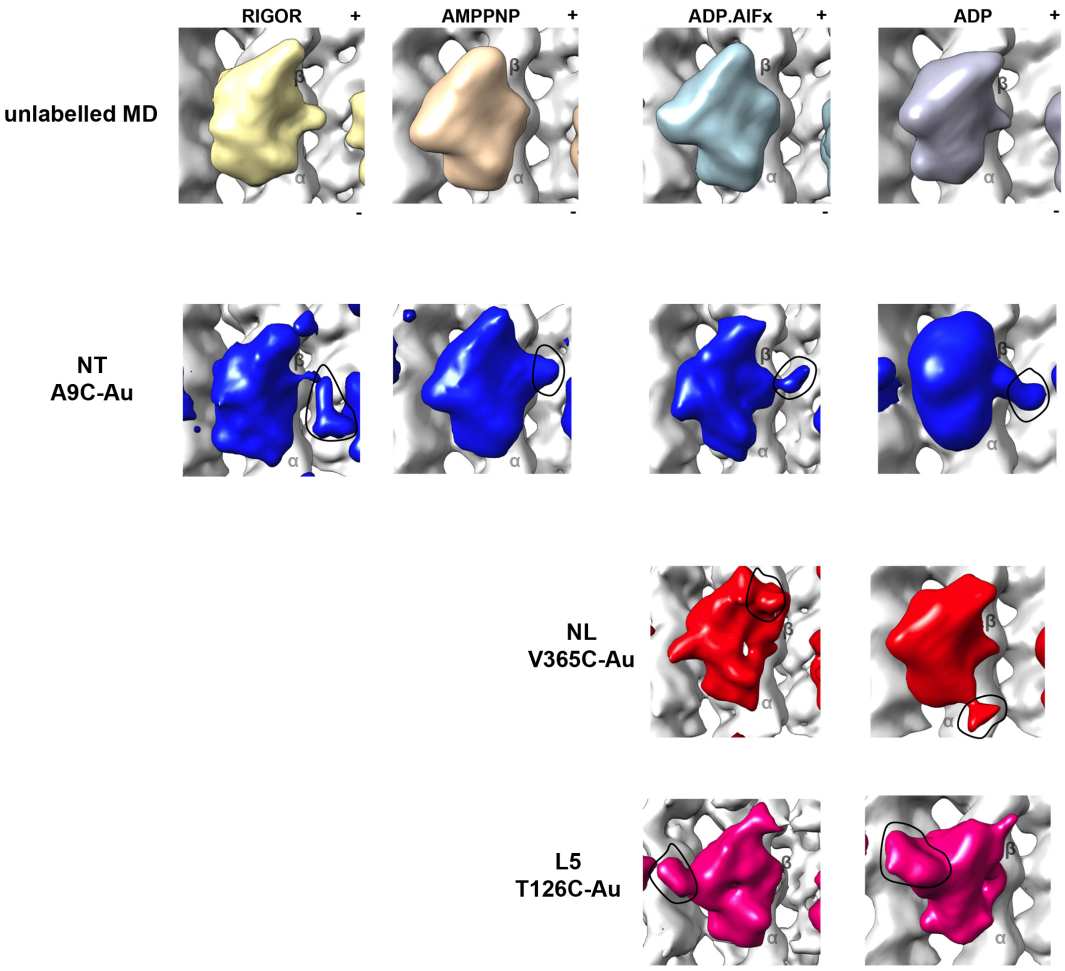

FIGURE S2. Comparison between unlabelled and gold-labelled K5 MD reconstructions. Surface views of all K5 MD reconstructions in (from left to right) rigor, AMPPNP (from (3)), ADP.AlFx and ADP states are shown. Unlabelled K5 MD reconstructions (top row) are filtered to match the lower resolution of the reconstructions calculated using gold-labelled K5 MD: A9C-Au in blue, V365C-Au in red, T126C-Au in pink. Structures are band-pass filtered in the range 30-16Å (according to the final resolution, Table S1), and contoured to account for the volume of the complex. Positions of gold densities in a single MD are outlined and the MT plus-end is towards the top.

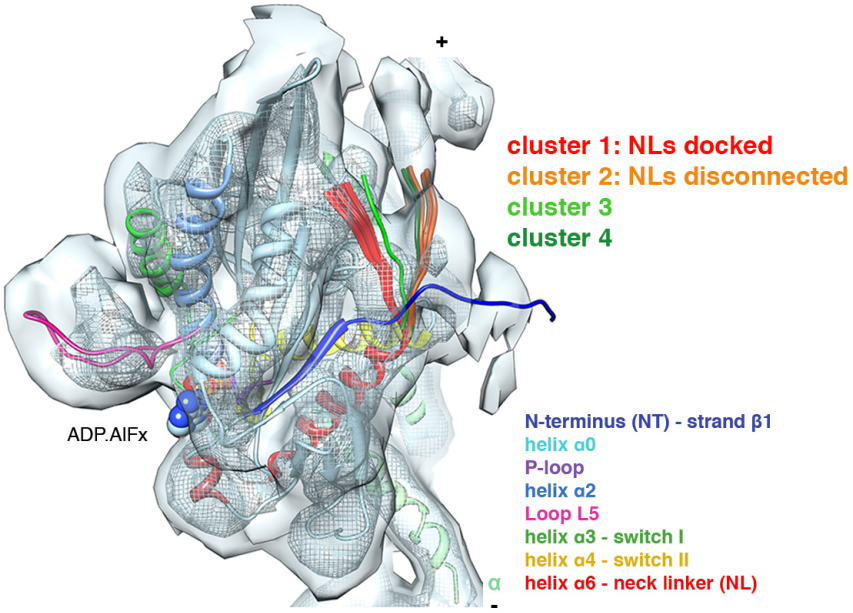

FIGURE S3. Visualization of NL destabilisation on initiation of ATP hydrolysis. Pseudo-atomic models of human K5 MD (color-coded as in the key) bound to an αβ-tubulin dimer (green ribbon) docked into the ADP.AlFx cryo-EM reconstruction contoured as in Fig. 1. The 44 NL conformers produced by energy minimisation that satisfy the gold density formed four clusters based on a RMSD Cα cut-off of 0.35Å: two of these correspond to 1) the docked NL conformation (red ribbons, 31 members) and 2) the disconnected NL conformation (orange ribbons, 9 members). The third cluster is close to the second (dark green, 3 members), and the last conformer lies between the docked and undocked conformations (light green, 1 member).

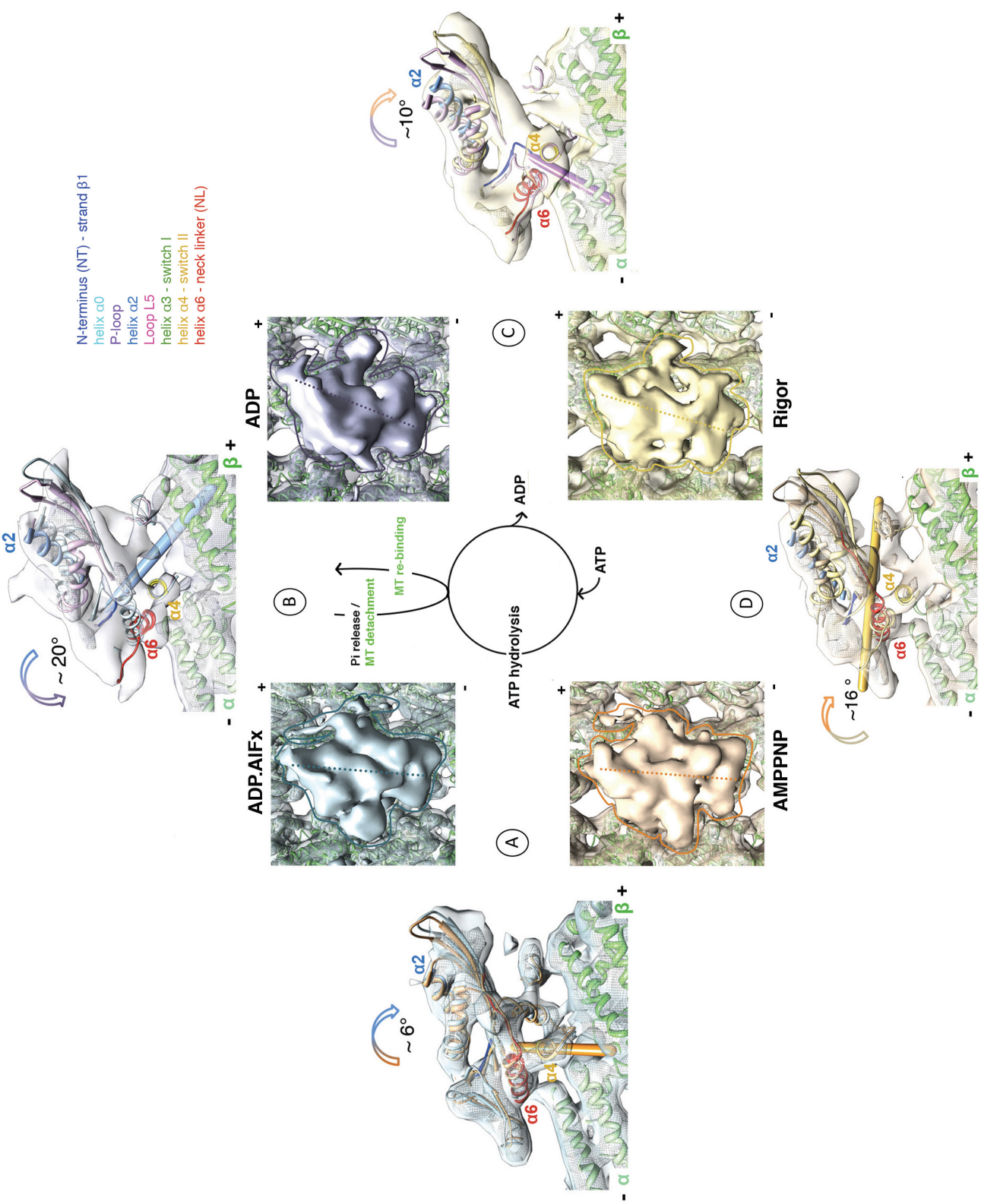

FIGURE S4. Global movements of the human K5 MD during its MT-based ATPase cycle. The central schematic illustrates steps in the ATPase cycle with the

associated conformational states: ATP hydrolysis (A), Pi release/MT detachment and MT re-binding (B), ADP release (C) and ATP binding (D). For each nucleotide state, front views of an αβ-tubulin dimer (green ribbon) with bound K5 MD are shown to illustrate the large scale conformational changes that occur at each step: AMPPNP (coral); ADP.AlFx (blue); ADP (purple); rigor (yellow). The MT plus-end is towards the top and K5 MDs are outlined. In the outside panels, conformational changes in the pseudo-atomic coordinates (color-coded as in the key) at each step are compared and docked into the cryo-EM density. In these side views, the MT plus-end is towards the right. The directions of MD rotations/tilts are indicated with color-coded arrows while the rotational axis of each conformational change is indicated by a colored rod. Front view reconstructions are displayed at a threshold equivalent to the molecular weight of the complex, while side view reconstructions are contoured at a higher threshold to most clearly show the rotations as follows: AMPPNP (surface contour: 1σ (front view) and 1.8σ (side view), mesh contour: 3σ); ADP.AlFx (surface contour: 1.1σ (front view) and 2σ (side view), mesh contour: 3.25σ); ADP (surface contour: 1.56σ (front view) and 2σ (side view), mesh contour: 3.4σ); rigor (surface contour: 0.94σ (front and side views), mesh contour: 3σ).

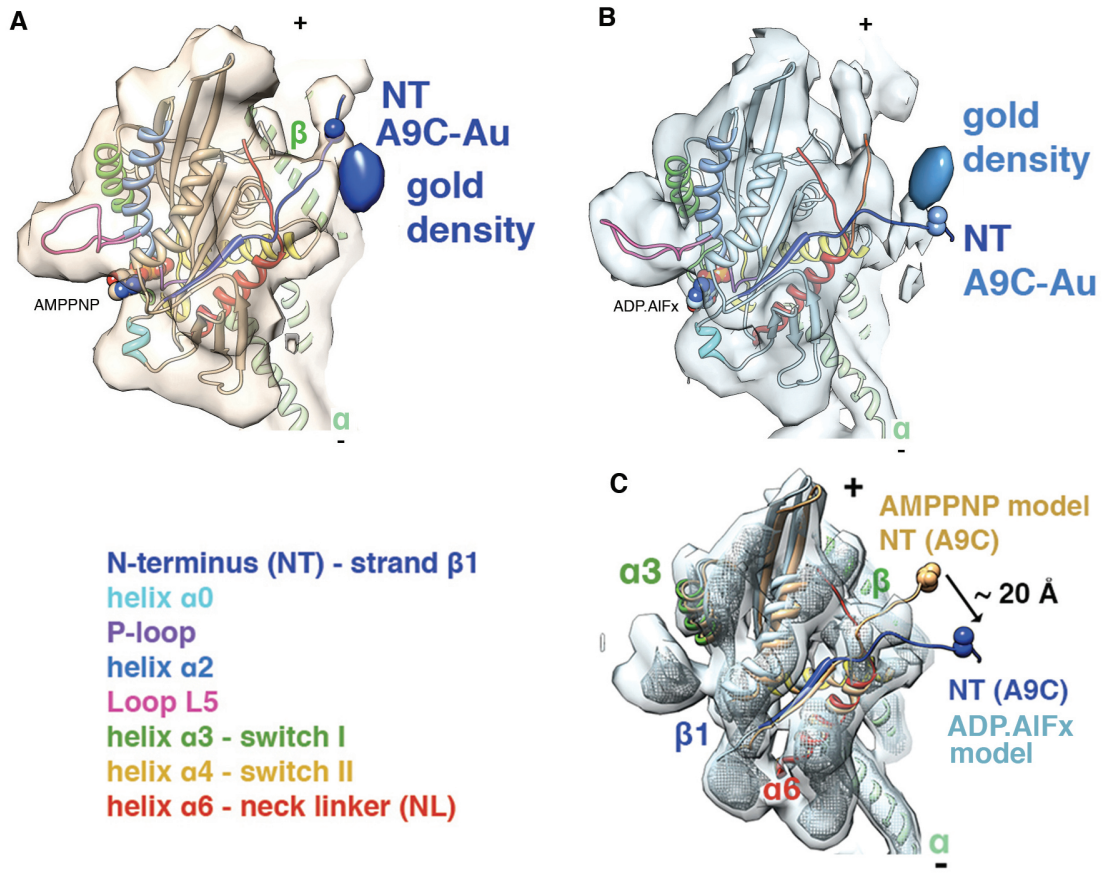

Figure S5. K5 N-terminus gold labelling (A9C) in the AMPPNP and ADP.AlFx states. (A,B) Difference maps of gold densities (gold covalently attached to the N-terminus via A9C) are superimposed onto the native cryo-EM reconstruction (contoured as in Fig. S3) in which pseudo-atomic models are docked (color-coded as in the key). Residues A9C are shown in space-filling representation and gold densities are contoured at 2.2σ (AMPPNP (A), dark blue) and 2.3σ (ADP.AlFx (B), light blue). **(C)** AMPPNP and ADP.AlFx models are superimposed on helices α4 and docked into the ADP.AlFx reconstruction. The surface is contoured at 2σ and only some of the secondary structural elements are shown for clarity. The ~ 20Å displacement of the N-terminus upon ATP hydrolysis is estimated based on the position of the residues A9C (space-filling representation).

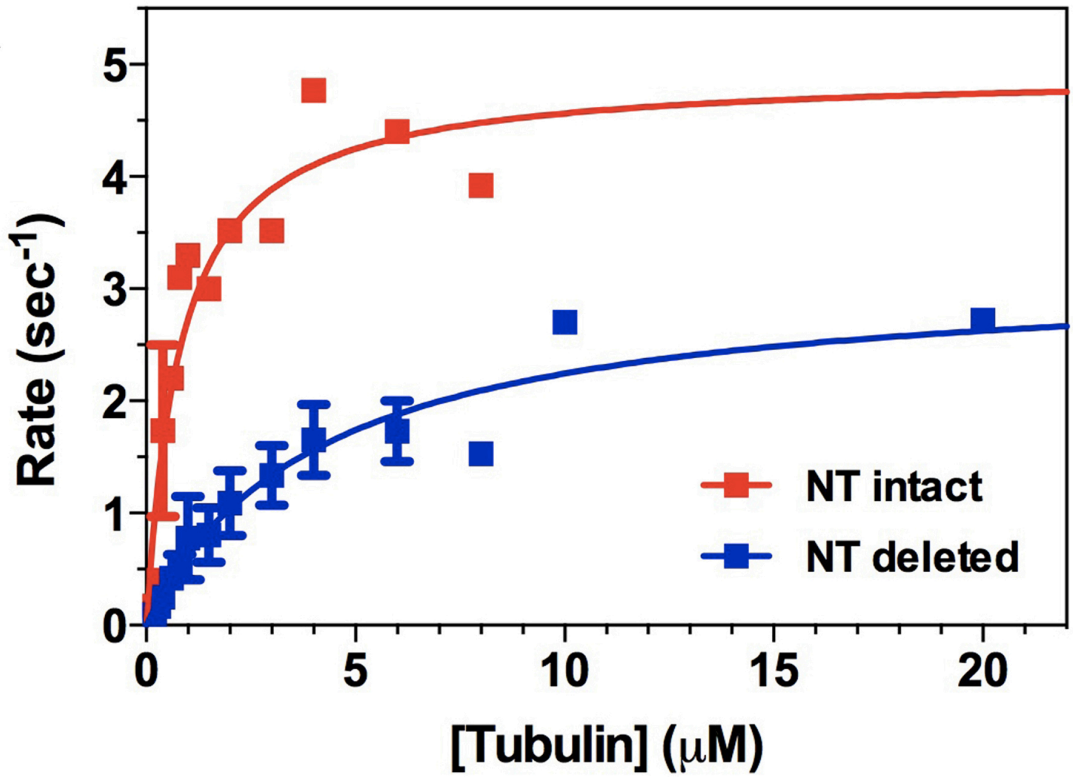

Figure S6: The effect of deletion of the N-terminus on kinetic parameters of the human K5 ATPase cycle. Steady state MT-activated ATPase activities of the *NT Intact* and *NT Deleted* constructs. The reaction was initiated by adding ATP to 2 mM. The dependence of measured rate of inorganic phosphate production on [MT] was fitted to a Michaelis-Menten relationship, defining values of k_{cat} and $K_{0.5,MT}$ of 4.9 ± 0.5/s and 0.81 ± 0.26 μM for *NT Intact* and 3.2 ± 0.4/s and 4.1 ± 1.1 μM for *NT Deleted*, respectively.

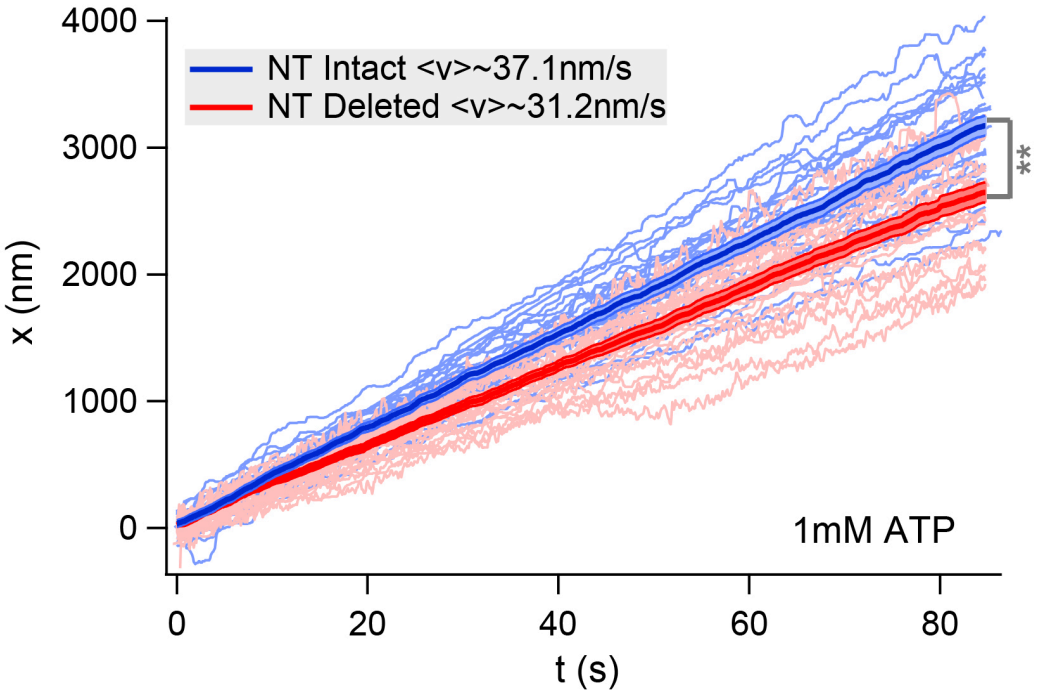

FIGURE S7. Effect of deletion of human K5 N-terminus on gliding motility. Individual MT gliding traces for *NT Intact* (blue) and *NT Deleted* (red) constructs in the presence of 1mM ATP. Each set of traces (N=31 and 27, respectively) were averaged together pointwise to extract average behavior (blue (37.1 nm/s) and red (31.2 nm/s) traces with error bars, which are SEM). In this trial, neither the *NT Deleted* nor *NT Intact* samples had a significant number of paused MTs.

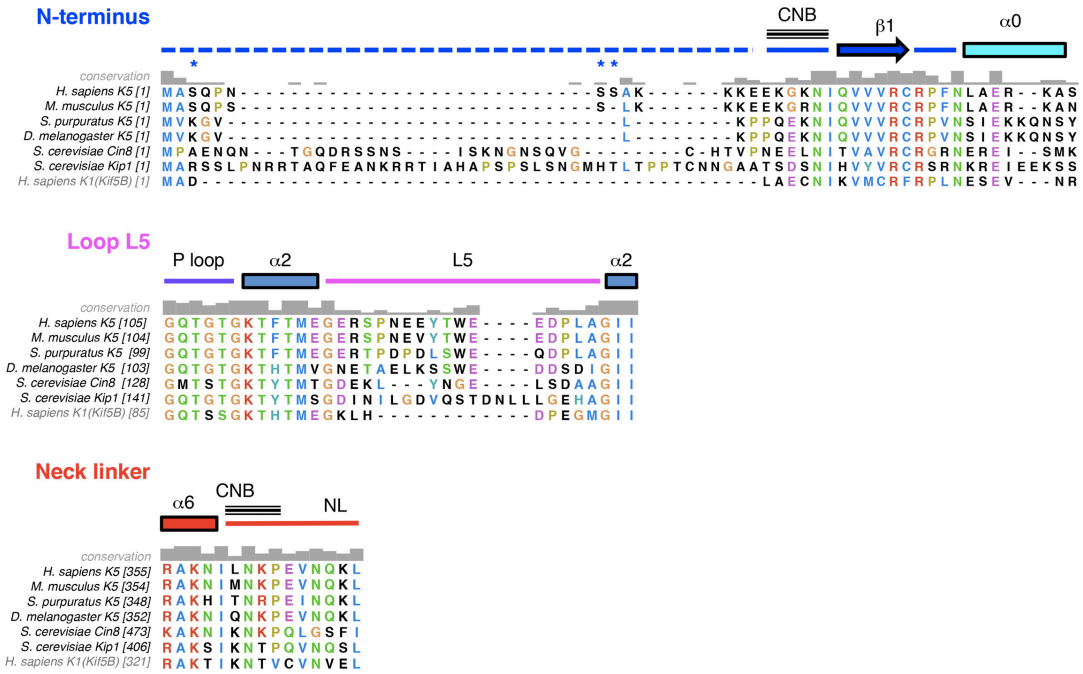

Figure S8. Sequence comparison between K5/K1 MDs illustrating conservation and divergence of the key regulatory regions. The associated secondary structural elements are indicated above the sequences. The parts of the N-terminus and NL involved in cover neck bundle formation (CNB) are indicated. Conserved regions include β1 (blue), the P loop (purple), most of α2 (grey blue) and the C-terminal end of α6 (red), while regions of sequence divergence amongst K5s and compared to K1 (labeled in grey) are the N-terminus (blue), α0 (cyan), L5 (pink) and neck linker (red). Uniprot codes are: *H. sapiens* K5: P52732; *M. musculus K5*: Q6P9P6; *S. purpuratus* K5: Q9GQ58; *S. cerevisiae* Cin8: P27895; *S. cerevisiae* Kip1: P28742; *H. sapiens* K1/Kif5B: Q6P164. The numbers in [brackets] are the starting residues for each alignment segment. Blue * indicate residues in the N-terminus of human K5 that are predicted phosphorylation sites (GPS 2.1 Online (16); NetPhosK1 (17)). The alignment was generated using T-coffee (18) and displayed using Chimera (11).

SUPPLEMENTARY MOVIE LEGEND

Movie S1. Concerted movement of L5, NL and N-terminus throughout the K5 ATPase cycle: the ATP hydrolysis transition step.

Movie S2. Concerted movement of L5, NL and N-terminus throughout the K5 ATPase cycle: the ADP release step.

Movie S3. Gliding assay of *NT intact* K5 MD. MTs are recruited and moved by *NT intact* K5 MD. The original recording was 512X512, and 11.8 fps. To make motion obvious, the movies have been sped up, and are now viewed at ~0.7 fps. Due to size considerations, movies for demonstration were down-sampled to 256 X 256 pixels, though actual quantitation as presented in the text was performed on the full-size full frame rate movies.

Movie S4. Gliding assay of *NT deleted* K5 MD. MTs are recruited and moved by *NT deleted* K5 MD. Movies were prepared as for Movie S3.

REFERENCES

1. Rosenfeld SS, Xing J, Jefferson GM, & King PH (2005) Docking and rolling, a model of how the mitotic motor Eg5 works. *J Biol Chem* 280(42):35684-35695.
2. Behnke-Parks WM*, et al.* (2011) Loop L5 acts as a conformational latch in the mitotic kinesin Eg5. *J Biol Chem* 286(7):5242-5253.
3. Goulet A*, et al.* (2012) The Structural Basis of Force Generation by the Mitotic Motor Kinesin-5. *J Biol Chem*. 287(53):44654-44666.
4. Sindelar CV & Downing KH (2007) The beginning of kinesin's force-generating cycle visualized at 9-A resolution. *J Cell Biol* 177(3):377-385.
5. Sindelar CV & Downing KH (2010) An atomic-level mechanism for activation of the kinesin molecular motors. *Proc Natl Acad Sci U S A* 107(9):4111-4116.
6. Ludtke SJ, Baldwin PR, & Chiu W (1999) EMAN: semiautomated software for high-resolution single-particle reconstructions. *J Struct Biol* 128(1):82-97.
7. Frank J*, et al.* (1996) SPIDER and WEB: processing and visualization of images in 3D electron microscopy and related fields. *J Struct Biol* 116(1):190-199.
8. Grigorieff N (2007) FREALIGN: high-resolution refinement of single particle structures. *J Struct Biol* 157(1):117-125.
9. van Heel M, Harauz G, Orlova EV, Schmidt R, & Schatz M (1996) A new generation of the IMAGIC image processing system. *J Struct Biol* 116(1):17-24.
10. Lowe J, Li H, Downing KH, & Nogales E (2001) Refined structure of alpha beta-tubulin at 3.5 A resolution. *J Mol Biol* 313(5):1045-1057.
11. Pettersen EF*, et al.* (2004) UCSF Chimera--a visualization system for exploratory research and analysis. *J Comput Chem* 25(13):1605-1612.
12. Topf M*, et al.* (2008) Protein structure fitting and refinement guided by cryo-EM density. *Structure* 16(2):295-307.
13. Pandurangan AP & Topf M (2012) Finding rigid bodies in protein structures: Application to flexible fitting into cryoEM maps. *J Struct Biol*. 177(2):520-531.
14. Sali A & Blundell TL (1993) Comparative protein modelling by satisfaction of spatial restraints. *J Mol Biol* 234(3):779-815.
15. Fiser A, Do RK, & Sali A (2000) Modeling of loops in protein structures. *Protein science : a publication of the Protein Society* 9(9):1753-1773.
16. Xue Y*, et al.* (2008) GPS 2.0, a tool to predict kinase-specific phosphorylation sites in hierarchy. *Molecular & cellular proteomics : MCP* 7(9):1598-1608.
17. Blom N, Sicheritz-Ponten T, Gupta R, Gammeltoft S, & Brunak S (2004) Prediction of post-translational glycosylation and phosphorylation of proteins from the amino acid sequence. *Proteomics* 4(6):1633-1649.
18. Notredame C, Higgins DG, & Heringa J (2000) T-Coffee: A novel method for fast and accurate multiple sequence alignment. *J Mol Biol* 302(1):205-217.